

# HARDI Segmentation via Fourth Order Tensors and Anisotropy Preserving Similarity Measures

Sumit Kaushik · Jan Slovák

Received: date / Accepted: date

**Abstract** In this work, we discuss the higher order tensors appearing in high angular resolution diffusion tensor imaging and we have tested two segmentation methods, the Riemannian spectral clustering and the deformable models, using several projections of the 4th order tensors to the 2nd order ones, and diverse similarity measures on them. High angular resolution diffusion imaging has proved its effectiveness in modeling white matter brain structures along with the fiber intersection regions, which is of high importance in brain research. Along with other known projections, we observe that the diagonal components of the flattened 4th order tensors also live in the well known Riemannian symmetric space of symmetric positive definite matrices. We discuss and compare several natural approximations of the distance on the latter space to be used in clustering and segmentation algorithms. The results show that some of the projections unfold the geometry of the higher order tensors very well and we also propose the exploitation of the spherical linear interpolation spectral quaternion metric, which proves to be very effective. The latter claims are supported by experimental comparison of the effectiveness of our algorithms with the more usual logarithmic Euclidean and spectral quaternionic metrics, in particular in presence of noise. Our methods allow to distinguish individual objects in complex structures with high curvatures and crossings.

**Keywords** diffusion tensor imaging · Riemannian symmetric space · quaternions · similarity measures · dimension reduction · fourth order tensor

**Mathematics Subject Classification (2010)** 92C55 · 53B21

## 1 Introduction

This work addresses the problem of segmentation of the white matter fiber structures like corpus callosum, cingulum etc. Anatomy of these structures has clinical importance in diagnosing and observing the progression of neuro diseases. Following [1], the Diffusion Tensor Imaging (DTI) gained importance because of its better precision than the conventional Magnetic Resonance Imaging (MRI). Diffusion of water molecules in complex microstructures is described by Gaussian distribution. The Gaussian modeling provides positive definite second order tensors, [2], since diffusion is a physical process. Thus, the estimated second order tensors lie in the Riemannian symmetric space of symmetric positive definite matrices (SPD). For nearly two decades, several works used various metrics suitable for processing data in this geometric space [3,4,5,6,7,8]. At the same time, this approach is known for its inability to model heterogeneous regions where two or more fibers cross, merge or touch (intra voxel complexity).

There are two main approaches to the analysis of the data – the Apparent Diffusion Coefficients (ADC) profile, and the methods based on the q-space.

The intra voxel complexity of fibers has been modeled by the diffusion spectral imaging, [9], and the Q-ball, [10], both examples of q-space based methods. For segmenting the voxels, earlier techniques also used the scalar measure representation of tensors, but the lacking directional information produced inaccurate results. The works [11],[12] are

---

The first author has been supported by the grant MUNI/A/1138/2017 of the Masaryk University, the second author gratefully acknowledges support from the Grant Agency of the Czech Republic, grant Nr. GA17-01171S.

---

Masaryk University, Faculty of Science, Department of Mathematics and Statistics  
Kotlarska 2, 611 37 Brno, Czech Republic  
E-mail: sumitkaushik24@gmail.com, E-mail: slovak@muni.cz

based on the level-set and the geometric flow based DTI segmentation methods.

Based on the ADC profile, a model called High Angular Resolution Diffusion Imaging (HARDI), [13],[14], was proposed to describe the complexity of diffusion. In [15], the authors considered the representation of the Oriented Distribution Functions (ODFs) as a mixture of von Mises-Fisher distributions.

The work [16] showed that representing dMRI data can help in separating fiber tracts in 5D nonlinear space, which is not possible when dealing with the problem in 3D. The work [17] performs the segmentation in q-space using diffusion maps and the region based surface evolution of HARDI [18]. The works [19,20] showed that the square root reparametrization of ODFs lies on the unit Hilbert sphere in the (infinite dimensional) Riemannian manifold of probability measures. The data can be then mapped to low dimensions for clustering.

The work [21] employed the fuzzy class membership framework to deal with the partial volume issues which arise due to sharing of voxels by structures, e.g. cingulum with anisotropic corpus callosum and isotropic ventricles. The fuzzy membership can account for uncertainty in the decision of segmentation at a voxel, while the crisp segmentation produces inaccurate results. Based on sparse theory, the method called Sparse Subspace Clustering (SSC), [22,23], is able to deal with intersecting subspaces. In those works, the fiber bundles are supposed to lie in separate 1D/2D submanifolds, depending upon the number of intersecting fibers.

Higher order tensors can be used to model the underlying complex structures. These positive definite tensors of any order can be represented as homogenous polynomials, [24]. The advantage of using polynomial representation is that they allow linear transformation to spherical harmonic form representation, [27,26,25], and it is easy to find the maxima of the ADC profiles. As a result, the coefficients of higher order tensors project linearly to the lower order tensor coefficients, [26].

Only a limited number of works address segmentation of HARDI based data, in particular the higher order tensors. The works [27,28] provide mathematical evidence that non-Gaussian diffusion causes non-exponential signal decay. The ADC profiles are based upon exponential signal decay assumption. Thus, more than six degrees of freedom are redundant (as in DTI). The maximum of diffusivity has misalignment with actual fiber directions which is due to the b-value and the less known micro level interactions of water molecules with cellular components [28]. The later work [29] resolved this issue by aligning this mis match in the higher order ADC profiles using symmetric positive definite Cartesian tensors CT-ODF. The ADC profiles are popular clinically because of the observation that its value decreases with onset of ischemia [30]. The rotational invariants of the

high order tensors showed interesting potential for new biomarkers with better robustness, [31,32,33].

In segmentation applied to intersecting regions, the orientations of the individual tensors are not relevant, since we consider the region as a whole. Therefore, the key idea in the present work is to exploit the geometry of the 2nd order tensors to segment fields of higher order tensors. We propose a novel approach which does not need to blow up the dimensions of submanifolds because of the intra voxel complexity. We have considered the problem in the form of Riemannian manifold clustering. However, this approach requires an effective anisotropy preserving metric to accurately account for the degree of anisotropies in the presence of non-uniformity. Our approach currently uses the 4th order tensors in the experiments but the method should be extendable to higher orders. Our contributions include the following:

1. We exploit the observation that the diagonal components of the flattened 4th order tensors are positive definite. We utilize the fact that the components lie in a well known Riemannian symmetric space. We compare the effect of this projection with two other well known projections.
2. We deal with the important issue how to extract the fiber bundle structure over the image space. Spectral clustering is used, where the weight terms of the affinity matrix are designed to account for spatial continuity of the fiber structures. An algorithm is provided here to get the weight parameters for geodesic distance which effectively deals with wide range of configurations. We also suggest an effective adjustment to the spatial distance to increase the robustness of the method.
3. We modify the Spectral Quaternion (SQ) metric to Spherical Linear Interpolation (slerpSQ) metric. The reason is that slerpSQ produces smoother interpolating curve in the underlying geometric space and so it is closer to the geodesic distance. Our experiments reveal that slight improvement in the segmentation results speaks in favor of the slerpSQ.

This work also provides a survey on the behavior of three similarity measures on different projections from the 4th order to the 2nd order tensors. The segmentation methods based on the spectral clustering for intersecting fibers and the global curve evolution for curved fibers are used. Our experimental results show the effectiveness of the methods under extrinsic similarity metrics. We use a bank of synthetic images with various complexity of fibers and their intersections. For illustration, we also add segmentation on a real image.

## 2 Diffusion modeling

ADC profile estimation can be achieved using spherical harmonics and fitting higher order tensors to the spherical data obtained in various gradient directions.

The general Stejskal-Tanner formula for the observed signal strength in a pulse sequence (diffusive attenuation) and the related diffusion tensor coefficients are

$$S = S_0 \exp(-bD(g)),$$

$$D(g) = \sum_{j_1=1}^3 \sum_{j_2=1}^3 \sum_{j_3=1}^3 \cdots \sum_{j_n=1}^3 D_{j_1 j_2 j_3 \cdots j_n} g_{j_1} g_{j_2} g_{j_3} \cdots g_{j_n},$$

where  $D_{j_1 \cdots j_n}$  are the coefficients of  $n$ -th order, while  $g_j$  are components of the unit gradient vector  $g$ ,  $b$  is the diffusion weighting factor, and  $S_0$  is the signal acquired without any diffusion gradients. For example, in 3D  $g = (g_x g_y g_z)^T$  and we write  $D_{j_1 j_2 j_3 j_4}$  for the 4th order tensor in Einstein's notation (and all  $j_i$  are  $x, y$  or  $z$ ). The least square estimation doesn't ensure positive diffusion profile. Methods proposed in [34, 24, 35] ensure positive semi-definiteness of the tensors.

A  $k$ -th order tensor has got  $3^k$  coefficients. Under the required symmetry, however, the number of independent components is reduced to  $N_k = \frac{1}{2}(k+1)(k+2)$ .

One reason to use higher order tensors is that they encode the geometry of diffusion without requiring spherical harmonic transform to compute them from diffusion profiles. Another advantage is pointed out in [26]. Once coefficients of higher order tensor are evaluated, lower order tensor coefficients can be simply obtained by linear projections. The symmetric and positive tensors can be expressed as coefficients  $p_{ijk}$  of polynomial of degree 4 with homogeneity condition  $i+j+k=4$ . Here,  $i, j, k$  also represents the degree of monomials  $g_x^i g_y^j g_z^k$ . The coefficients of  $D$  and the polynomial coefficients satisfy the relation  $p_{ijk} = \frac{4!}{i!j!k!} D_{j_1 j_2 j_3 j_4}$ .

In our numerical experiments (in particular dealing with the synthetic data), we use the general framework proposed in [24] to estimate coefficients of positive definite tensor of any order.

In [21], the motivational illustration showed that it is not encouraging to use the Gaussian model for second order tensors directly, because mean of anisotropic tensors can be isotropic. In our method, in order to extract these regions properly, a similarity measure must be chosen which could discern between different anisotropic tensors.

## 3 The Projections

Appropriate mappings projecting the 4th order tensors into positive definite 2nd order tensors are required.

### 3.1 A Linear Projection of 4th Order Tensors to 2nd Order

One of good possibilities how to project the 4th order tensor was introduced in [26]. It is a simple linear relation but, unfortunately, it suffers a loss of orientation information. The expressions to evaluate independent coefficients of second order from the 4th order tensor come from the spherical harmonics representations of the Laplace series for the coefficients of  $D$  and best data fitting.

$$D_{xx} = \frac{3}{35}(9D_{xxxx} + 8D_{xxyy} + 8D_{xxzz} - D_{yyyy} - D_{zzzz} - 2D_{yyzz})$$

$$D_{yy} = \frac{3}{35}(9D_{yyyy} + 8D_{xxyy} + 8D_{yyzz} - D_{xxxx} - D_{zzzz} - 2D_{xxzz})$$

$$D_{zz} = \frac{3}{35}(9D_{zzzz} + 8D_{xxzz} + 8D_{yyzz} - D_{xxxx} - D_{yyyy} - 2D_{xxyy})$$

$$D_{xy} = \frac{6}{7}(D_{xxyy} + D_{yyyx} + D_{zzxy})$$

$$D_{xz} = \frac{6}{7}(D_{xxxz} + D_{zzzx} + D_{yyxz})$$

$$D_{yz} = \frac{6}{7}(D_{yyyz} + D_{zzzy} + D_{xxyy}).$$

The details can be found in [26]. In the sequel, we write  $L$  for this projection.

### 3.2 Decomposition of Flattened 4th Order Tensors

In material science, it is common to use 6D second order tensor representation for classification of materials and it was proposed to be used in DTI application in [36]. This isomorphic mapping can be viewed as an isometry, [37]. The  $6 \times 6$  representation however leads to loss of angular features, [38]. Another disadvantage is that it is not possible to represent 6D rotation using quaternions as employed in the spectral approach discussed below.

Flattening of the tensor comes naturally by considering matrix generalization of scalars and viewing  $\mathbb{R}^{3^n}$  as

$$\mathbb{R}^{3^n} = \mathbb{R}^{3^{n-2}} \otimes \mathbb{R}^{3^2}.$$

This identity retains geometry of underlying fibers and it is an isometry too. It enjoys the symmetric positive semi-definite property. Thus, a general  $n$ th order tensor  $T^{(n)}$  can be expressed as a matrix of  $(n-2)$ nd order tensors:

$$T^{(n)} = \begin{pmatrix} T_{xx}^{(n-2)} & T_{xy}^{(n-2)} & T_{xz}^{(n-2)} \\ T_{yx}^{(n-2)} & T_{yy}^{(n-2)} & T_{yz}^{(n-2)} \\ T_{zx}^{(n-2)} & T_{zy}^{(n-2)} & T_{zz}^{(n-2)} \end{pmatrix}$$

and, for example the left upper corner element in the 4th order tensor is

$$T_{xx}^{(2)} = \begin{pmatrix} D_{xx(xx)} & D_{xx(xy)} & D_{xx(xz)} \\ D_{xx(xy)} & D_{xx(yy)} & D_{xx(yz)} \\ D_{xx(xz)} & D_{xx(yz)} & D_{xx(zz)} \end{pmatrix}.$$

For symmetric fourth order tensors, there are 15 independent coefficients  $D_{ijkl}$ , where the subscripts take values  $x, y, z$

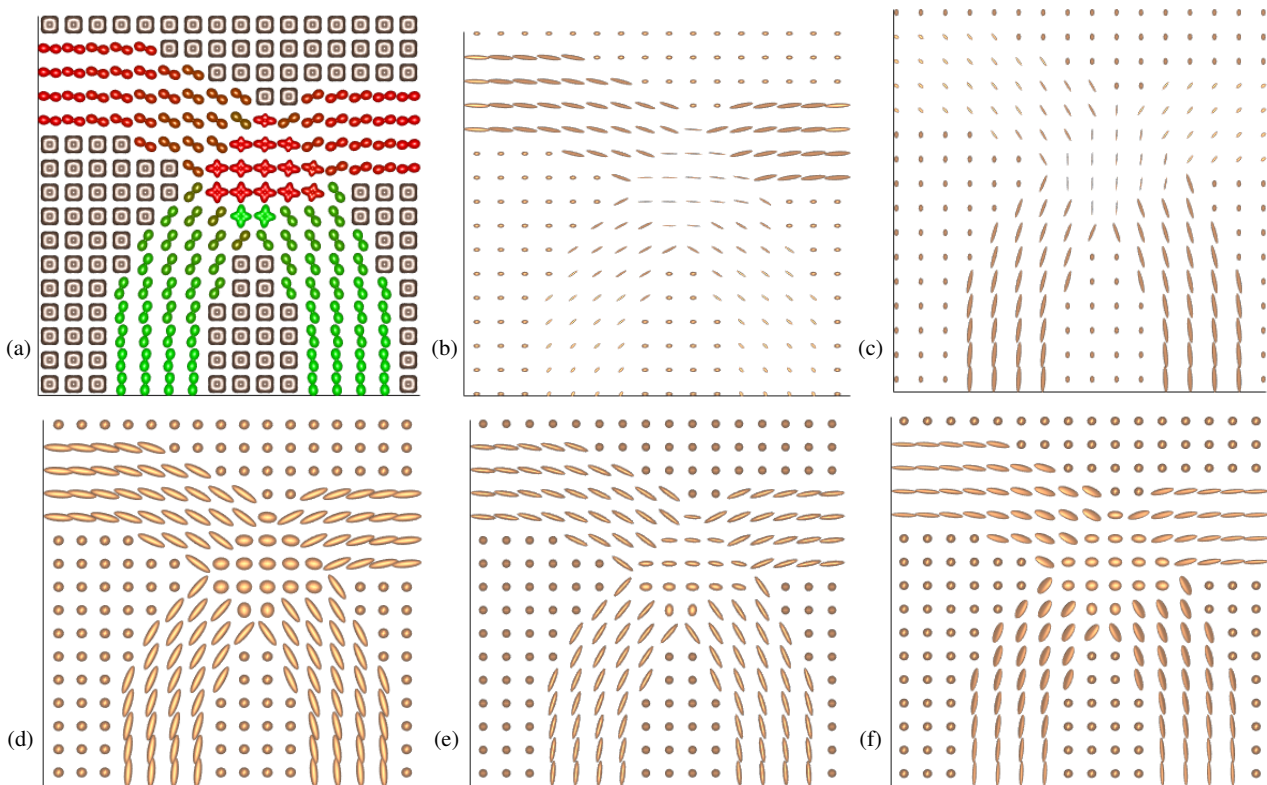


Fig. 1: (a) curved fiber intersection (synthetic data), (b)  $x$ -diagonal component, (c)  $y$ -diagonal component, (d) sum of  $x$  and  $y$  diagonal components, i.e. the  $D$  projection (e) the  $E$  projection, (f) the  $L$  projection

with repetitions allowed. The coefficients can be estimated considering any even order tensor equivalent to homogenous polynomials in three variables, [24].

Notice that if  $n = 4$ , the result is a  $9 \times 9$  symmetric matrix. Three of its eigenvalues are zero due to linear dependencies and there are the six further eigen vectors, all with positive eigenvalues, [38]. The components of the principal eigen vector, corresponding to maximum eigenvalue, form a second order tensor called Eigentensor. The work [38] showed that such six independent eigentensors have the potential to reveal multifiber directions.

We call the projection to the principal Eigentensor  $E$ .

### 3.3 The Diagonal Components

The diagonal components obtained above retain geometrical information of the full tensor as shown in Figure 1, (b) and (c). The empirical observation that the diagonal components themselves are SPDs can be easily checked theoretically. Indeed, the flattened 4th order tensor viewed as the  $9 \times 9$  matrix  $T$  with columns and rows ordered as dealing with a decomposable tensor  $T_{ijkl} = D_{ij}^1 D_{kl}^2$  with two second order tensors  $D^1$  and  $D^2$ , displays the same symmetries as the flattened symmetric  $3 \times 3$  matrices. This means the 4th

column copies the 2nd one, the 7th copies the 3rd one, the 8th copies the 6th one, etc. Thus the eigenvectors of  $T$  will again enjoy the structure of flattened  $3 \times 3$  symmetric matrices. Three of them will be zero (due to the repetition of some columns) and the remaining six ones correspond to the eigenvalues of the  $6 \times 6$  matrix  $T'$  obtained from  $T$  by forgetting the repeated columns.

At the same time, the positive eigenvalues from the above spectral decomposition coincide with those 6 eigenvalues of  $T'$ . In particular we know that  $T'$  is positive definite and thus, by the Sylvester criterion, all the principal minors of  $T'$  are positive. In particular, the top left symmetric  $3 \times 3$  matrix must be a SPD. Finally, the same must be true for the remaining diagonal blocks since the ordering of the blocks is given by our preferred order of coordinates, so it cannot have any impact on their properties.

Notice, a sum of two positive definite quadratic forms is again positive definite and so any linear combination of the diagonal SPDs with positive coefficients is positive definite, too. In 2D field representation, we consider the sum of the  $T_{xx}^{(2)}$  and  $T_{yy}^{(2)}$  components, i.e. a field of SPDs.

In the sequel, this projection will be denoted by  $D$ .

Figure 1 illustrates the behavior of all the above mentioned projections on a simple fiber crossing case. For cross-

ing regions the cluster of second order tensors is to be segmented as a separate region, but we want to see the other two disjoint parts of the same fiber in one region.

The synthetic images are created by a simulation of the signal generated with  $b = 1500s/mm^2$  and  $S_0 = 1$  with 21 gradient directions uniformly distributed over the sphere. Adaptive kernel method is used to create two fiber configurations as in [39]. The positivity of the higher order tensors is maintained according to [34]. The orientation of the fibers is color coded.

#### 4 Metrics on the Space of Symmetric Positive Definite Matrices

The Symmetric Positive Definite (SPD) matrices form a manifold carrying the structure of a Riemannian symmetric space. Geometrically, these matrices form the cone  $\mathbb{S}_n^+$  in  $\mathbb{R}^{n^2}$ , a manifold carrying an intrinsic Riemannian metric. We are interested in the case of  $n = 3$ , where the dimension of  $\mathbb{S}_3^+$  is six.

##### 4.1 Useful Metrics on $\mathbb{S}_n^+$

*Affine Invariant metric.* The space  $\mathbb{S}_n^+$  comes equipped with the natural action of the general linear group  $\mathbb{GL}(n)$ , well known from the algebra of quadratic forms. If  $g \in \mathbb{GL}(n)$  and  $p \in \mathbb{S}_n^+$ , then the action is

$$p \mapsto gpg^T.$$

Thus,  $\mathbb{S}_n^+$  is a homogeneous space. If we restrict the action to the orthogonal subgroup  $\mathbb{SO}(n)$  in  $GL(n)$ , then the action is still transitive and each of its orbits contains exactly one diagonal matrix, up to the ordering of the diagonal elements. Requesting a metric invariant with respect to this action, we have to define it in terms of distance  $N(p)$  of the matrix from the identity, while the general distance function should be

$$\text{dist}(p, q) = N(p^{-1}q).$$

Remind,  $\mathbb{S}_n^+$  is the isomorphic exponential image of the vector space of all symmetric matrices. This suggests to define

$$N(p)^2 = \|\log p\|^2 = \sum_{i=1}^n (\log \sigma_i)^2,$$

where  $\sigma_i$  are the eigenvalues of  $p$ , i.e. the diagonal elements of the unique diagonal matrix in the orbit of  $p$ .

Indeed, this provides a well defined Riemannian metric which is extremely important and widely used in both theory and practice, cf. [3,4,5]. Unfortunately, for our purposes, this metric is computationally too expensive and, moreover, it does not allow to handle the isotropy and rotation part separately. Therefore, there are many known approximations of this metric which are effectively used in practical problems.

*The Log-Euclidean metric.* Matrix exponential is a diffeomorphism from the space of all symmetric matrices in the embedding space  $\mathbb{R}^{n^2}$  to our 2nd order tensor space  $\mathbb{S}_n^+$ . The authors of [40] suggested a commutative Lie group structure on  $\mathbb{S}_n^+$  by taking only the linear terms in the matrix product expression via the logarithm:

$$p_1 \bullet p_2 = \exp(\log(p_1) + \log(p_2)) \quad (1)$$

$$\text{dist}(p_1, p_2)^2 = \text{trace}((\log(p_1) - \log(p_2))^2), \quad (2)$$

while the shortest interpolation curve between two tensors  $p_1$  and  $p_2$  is

$$p(t) = \exp((1-t)\log(p_1) + t\log(p_2)), \quad t \in [0, 1]. \quad (3)$$

This extrinsic metric is an approximation of the intrinsic affine invariant metric and it is a very popular metric in DTI processing. We shall call it LogE. It is invariant to similarity transformation (scaling followed by rotation or translation). LogE interpolation curve given by (3) provides a closed form mean for two or more tensors.

Thus, the computations of distances and means become easy in three steps: Take mapping log from the tensor space  $\mathbb{S}_n^+$  to the euclidean space of symmetric matrices, process the mapped data (symmetric matrices) there, finally use the exponential map exp to map the data back to the manifold  $\mathbb{S}_n^+$ .

*The Spectral metric.* For the first time, [41] used the spectral treatment for regularization of noisy diffusion tensors. The key idea is to treat eigenvalues and eigenvectors of a SPD matrix separately. Let us restrict to the space  $\mathbb{S}^+$  in dimension 3.

If we restrict the group acting on  $\mathbb{S}^+$  to the special orthogonal group  $\mathbb{SO}(3)$  (the group of all rotations in  $\mathbb{R}^3$  with the axis through the origin), then the matrix transposition coincides with the inverse and we may write the 2nd order tensors as  $p = u\Lambda u^T$  with  $u \in \mathbb{SO}(3)$  and  $\Lambda$  a diagonal matrix containing all the eigenvalues of  $p$ . Thus, we may consider the tensors in  $\mathbb{S}^+$  as couples  $(u, \Lambda)$  and write the interpolation curve between any two tensors  $p_1 = (u_1, \Lambda_1)$  and  $p_2 = (u_2, \Lambda_2)$  as

$$p(t) = u(t)\Lambda(t)u(t)^T \quad (4)$$

$$u(t) = u_1 \exp(t \log(u_1^T u_2)) \quad (5)$$

$$\Lambda(t) = \exp((1-t)\log(\Lambda_1) + t\log(\Lambda_2)). \quad (6)$$

This interpolation curve is a geodesic in the space of the Lie group  $G = \mathbb{SO}(3) \times \mathbb{D}^+(3)$ , where  $\mathbb{D}^+(3)$  is the group of diagonal matrices with positive elements. This Lie group is a 4-1 covering of  $\mathbb{S}^+$ , i.e. there is a locally invertible map  $G \rightarrow \mathbb{S}^+$ , such that each image point has got exactly four preimages.

These preimages of  $p$  differ by three distinct orientations originated by rotation by angle  $\pi$  around the principle axes

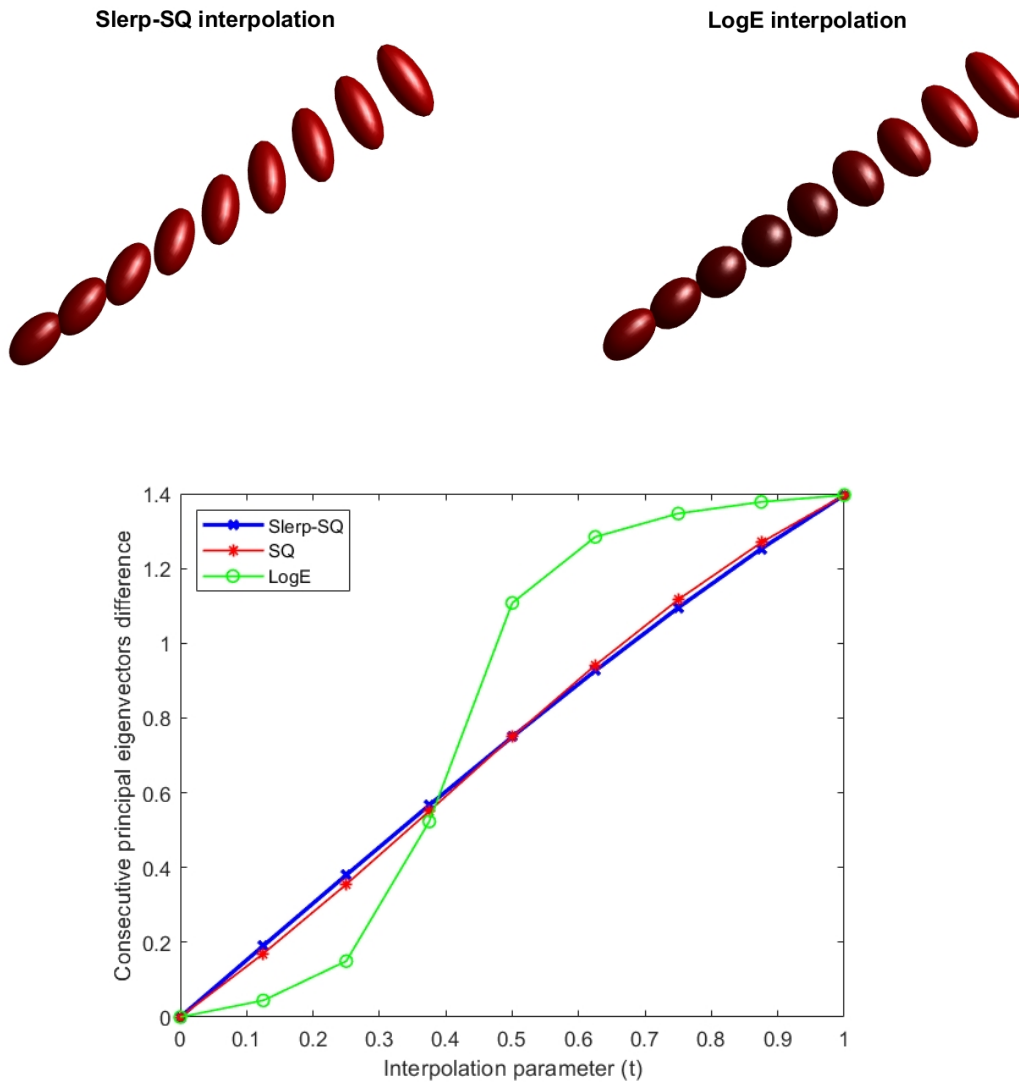


Fig. 2: The pictures show the interpolation between two anisotropic tensors (depicted as ellipsoids in 3D) with eigenvalues  $(15, 5, 5)$  and  $(25, 5, 5)$  and angular difference  $\frac{4}{3}\pi$  between the principal eigenvectors; the two pictures on the first line illustrate the loss of anisotropy via the LogE metric (on the right), while the slerpSQ is very satisfactory (on the left); the other picture shows the angular difference of principle eigenvectors for the  $n = 8$  values of the interpolation parameter along the horizontal axis. Notice the optimal behavior of the slerpSQ case, only slight difference between the slerpSQ and SQ metrics, and the failure of the LogE one.

of the ellipsoid associated to the SPD  $p$  and one due to the identity. Let  $U$  be one such 4-tuple associated to  $u_2 \in \mathbb{SO}(3)$ . Then the distance between the rotations  $u_1$  and  $u_2$  is defined as

$$\text{dist}(u_1, u_2) = \min_{u \in U} \text{dist}(u_1, u) = \min_{u \in U} \|\log(u_1 u^T)\|. \quad (7)$$

The calculations here require four matrix exp and log operations.

The distance on  $\mathbb{D}^+(3)$  is defined as in the Euclidean Log approach and we may consider the product metric on  $\mathbb{SO}(3) \times \mathbb{D}^+(3)$ .

#### 4.2 The Spectral Quaternion and the Spherical Linear Interpolation Spectral Quaternion Metric

The spectral quaternion (SQ) metric, [42], is based on the linear interpolation and it uses an inner-product based metric for rotation space (coming from the natural scalar product on quaternions). Essentially, this is the above discussed spectral metric, handled via the 2-1 covering of the orthogonal group by unit quaternions. The Hopf-Rinow-De Rham theorem indicates that among all possible geodesics between any two points on a complete Riemannian manifold there exists at

least one geodesic with minimum length which can be considered as distance between two points.

We propose a modification of the SQ metric, the so called spherical interpolation spectral quaternionic (slerpSQ) metric. Motivated by the techniques in robotics and animation, we define the slerpSQ interpolation  $q_m$  between two unit quaternions  $q_1$  and  $q_2$  as follows. First we posit

$$\theta = \arccos(|q_1 \cdot q_2|), \quad \theta \in [0, \pi/2],$$

where  $\cdot$  means the standard scalar product on quaternions, and then we define ( $q_1 \neq \pm q_2$ )

$$q_m(q_1, q_2, t) = \frac{\sin((1-t)\theta)}{\sin \theta} q_1 + \frac{\sin(t\theta)}{\sin \theta} q_2. \quad (8)$$

Notice  $\theta$  defines distance on the sphere of the unit quaternions, cf. [43]. We denote it  $d_{\text{slerpSQ}}$ . The interpolation (8) is defined as the constant speed path along the principal circle on the sphere of unit quaternions and it allows for effectively computing weighted means  $q_m$  for any finite number of tensors. Notice the computational advantage of skipping the renormalization step compared to SQ.

Let us notice that SQ and slerpSQ are topologically equivalent distances on the unit quaternions, [43],

$$d_{\text{SQ}}^2 = 2(1 - \cos(d_{\text{slerpSQ}})).$$

The SQ metric evaluates essentially the chordal distance of quaternions on the unit sphere. However, these two distances are not bounded equivalent since  $d_{\text{SQ}}(q', q)$  converges to 0 at a slower rate than  $d_{\text{slerpSQ}}$  if  $q' \rightarrow q$ , [43].

Both  $d_{\text{SQ}}$  and  $d_{\text{slerpSQ}}$ , when considered on unit quaternions are actually only pseudometrics (e.g. the slerpSQ distance of  $q$  and  $-q$  is zero), but this ambiguity disappears once we project to the rotation group.

Slerp also produces smoother curves in quaternion space and the resulting geodesics are closer to the geodesic distance in the Lie group  $\mathbb{S}\mathbb{O}(3) \times \mathbb{D}^+(3)$ . Figure 2 shows this behavior and compares to much worth performance of the LogE metric. Actually, the interpolation shown at the Figure 2 combines the difference in the rotational part and the eigenvalue part, taking them with the same weights for both SQ and slerpSQ. In general, this requires special attention, see below.

### 4.3 Similarity Measures and Algorithms

Anisotropy carries useful information and requires to be preserved during processing of second order tensors in many applications (e.g. in brain research). More importantly, for our purposes, the true distance between two tensors  $p_1$  and  $p_2$  should be rather a weighted combination  $d_\Lambda + \alpha d_Q$  of the  $\mathbb{D}^+(3)$  distance of the components  $\Lambda_1$  and  $\Lambda_2$  and the distance of the rotational components  $u_1$  and  $u_2$  (where we

consider either  $d_Q = d_{\text{slerpSQ}}$  or  $d_Q = d_{\text{SQ}}$ ). The smaller the anisotropy is, the less relevant is the rotational component.

To account for the tensors with negligible difference between the maximal and minimal eigenvalues, a smooth transition function is proposed in [42] (in our experiments, we use the value  $\beta = 0.6$ ):

$$f(x) = \frac{(\beta x)^4}{1 + (\beta x)^4},$$

to be combined with the so called Hilbert Anisotropy

$$HA(p) = \log \frac{\lambda_{\max}}{\lambda_{\min}},$$

reflecting the difference between the maximal and minimal eigenvalues of the symmetric positive definite matrix  $p$ . The weighting function is then defined by

$$\alpha(p_1, p_2) = f(\min(HA(p_1), HA(p_2))). \quad (9)$$

The LogE metric simply provides the approximation to the distance of two tensors and does not allow for distinguishing the eigenvector and eigenvalue parts, which is the advantage of the spectral decomposition. Working with SQ or slerpSQ, we evaluate the similarity measure by the Algorithm 2 below. This similarity measure is not a distance between two tensors but it provides a good approximation respecting the anisotropy.

We need to compute the weighted means with respect to the above metrics. Remind that there are four rotations representing a given tensor, so using quaternions to deal with them, we arrive at eight quaternions  $q$  associated to a given tensor  $p$ . We shall write  $Q$  for this set of eight associated quaternions.

#### Algorithm 1. Weighted Mean

*Input:* Set of tensors  $p_i$ ,  $i = 1, \dots, N$ , with weights  $w_i$ , such that  $\sum w_i = 1$ .

*Output:*  $p_\mu$ , the mean tensor.

1. Find the spectral decomposition of all  $N$  tensors,  $p_i = u_i \Lambda_i u_i^T$  and get quaternions  $q_i$  representing  $u_i$ .
2. Evaluate the three components of the weighted mean  $\Lambda_\mu$  of the eigenvalue part,  $\lambda_{\mu,k} = \exp(\sum_{i=1}^N w_i \log(\lambda_{i,k}))$ ,  $k = 1, 2, 3$ .
3. Select the reference quaternion  $q^{\text{ref}}$  of the tensor which maximizes  $w_i HA(p_i)$ ,  $i = 1, \dots, N$ .
4. With respect to  $q^{\text{ref}}$ , the realigned quaternions are given by  $q_i^a = \arg \min_{q_i \in Q_i} \arccos(|q^{\text{ref}} \cdot q_i|)$ .
5. If dealing with slerpSQ, then the weighted mean  $q_\mu$  is given by the equation (8) (modified for  $N$  elements), i.e.  $q_\mu = q_m$ . If we consider the SQ metric then we set  $q_m = \arg \max_{q_i \in Q_i} (q^{\text{ref}} \cdot q_i^a)$  and normalize to  $q_\mu = \frac{q_m}{|q_m|}$ .
6. Compute rotation matrix  $u_\mu$  from  $q_\mu$ .
7. Finally,  $p_\mu = u_\mu \Lambda_\mu u_\mu^T$ .

**Algorithm 2.** Distance Approximation*Input:* Tensors  $p_1$  and  $p_2$ .*Output:* The distance (similarity measure)  $\text{dist}(p_1, p_2)$ .

1. Find spectral decomposition of the tensors and get quaternions representing their rotation matrices.
2. The distance between eigenvalues is given by:  
 $d_\Lambda^2 = \exp(\sum_i |\log \frac{\lambda_i(p_1)}{\lambda_i(p_2)}|^2)$ .
3. The weighting factor is given by:  $\alpha(p_1, p_2) = f(x)$  by equation (9), where  $x = \min(HA(p_1), HA(p_2))$ .
4. With  $q_1$  as the reference quaternion, the realigned quaternion is calculated as  $q_2^a = \arg \min_{q_2 \in Q_2} \arccos(|q_1 \cdot q_2|)$ , and  $d_{\text{slerpSQ}} = \arccos(|q_1 \cdot q_2^a|)$ , while  $d_{\text{SQ}} = \|q_1 - q_2^a\|$ .
5.  $\text{dist}(p_1, p_2) = \alpha(p_1, p_2)d_Q + d_\Lambda$ .

In all our experiments, we use algorithms 1 and 2 for evaluating mean and distance measures for both SQ and slerpSQ, respectively. When we compare with the LogE metric we use the obvious formulae instead of the latter algorithms.

The next algorithm computes the relevant normalization of the second order tensor data which will be essential below. Since we observe the log normal distribution on the tensor space, [44], we first transform the data into a vector space by the matrix logarithm, then we compute the standard variance and finally transform this variance to the original log normal distribution.

**Algorithm 3.** Variance of SPD Tensors*Input:* The  $N$  second order tensors  $t_i, i = 1, \dots, N$ .*Output:* The variance  $w$ .

1. Take matrix logarithms  $\log t_i$  of the data  $t_i$ .
2. Compute the arithmetic mean of the matrices  $\log t_i$   
 $\mu = \sum_{i=1}^N \frac{\log t_i}{N}$ .
3. We set  
 $v = \left\| \sum_{i=1}^N \frac{(\log t_i - \mu)^2}{N} \right\|$ .
4. The back transformation provides  $w = \log\left(1 + \frac{v}{\|\mu\|^2}\right)$ .

**5 Segmentation Methods****5.1 Riemannian manifold clustering**

Clustering multiple sub-manifolds can be done through non-linear dimensionality reduction methods (NLDR). A set of points belonging to a non-linear manifold lying in higher dimensional (Euclidean) space can be mapped to lower dimension so that the distances in the projections mimic reasonably the original distances in the big space. Finally, the points mapped to lower dimension can be clustered using traditional methods like  $k$ -means.

The local NLDR techniques like Local Linear Embedding (LLE) and Hessian LLE, involve  $k$  nearest neighbors

( $k$ -NN). When dealing with bundles of fibers, the neighboring tensors may belong to different or the same fibers independent of their diffusion properties. Therefore, locality preserving Laplacian Eigenmap method (LE), [45], is used which does not involve evaluation of neighboring tensors.

The weights in the prospective affinity matrix are constructed by the following expression using both the appropriate similarity measure on the tensors and the spatial terms to account for the structural continuity of the fibers. The elements of the affinity matrix  $W \in \mathbb{R}^n \otimes \mathbb{R}^n$  measures similarity between the tensors at the voxels in the region of interest (the shape of  $W$  is motivated by the heat kernel, and  $n$  is the total number of points belonging to the region of interest)

$$w_{ij} = \exp\left(-\frac{\text{dist}(p_i, p_j)^2}{w_g} - \frac{\|i - j\|^2}{w_e}\right). \quad (10)$$

Here  $p_i$  and  $p_j$  are the tensor field values at the voxel positions  $i$  and  $j$ , respectively, while  $\|i - j\|$  is the modified Euclidean distance between the voxels,  $i \neq j$ ,  $\|i - j\|^2 = i_j + \frac{k}{i_j}$ , where  $i_j$  is the square of the Euclidean distance and  $k$  reflects the number of neighbors whose distance we want to blow up slightly. In our experiments we used  $k = 33$ . Moreover, in our experiments,  $w_e = 1$  and  $w_g$  is uniformly computed by Algorithm 3 above. This means we normalize the tensors  $p_i$  to have the variance one. Notice,  $w_{ii} = 1$  for all  $i$  while  $0 < w_{ij} < 1$  for all  $i \neq j$ .

The LE method is based on working with projections of  $n$  points into  $\mathbb{R}$  minimizing the objective function  $F = \sum_{i,j} (y_i - y_j)^2 w_{ij}$ , where  $y = (y_i)$  are the vectors of the prospective projections.

Clearly,  $F = 2y^T D y - 2y^T W y$  where  $D$  is the diagonal matrix with the diagonal element vector equal to the sum of all columns in  $W$ . Thus, we deal with the well known graph Laplacian

$$L = D - W \quad (11)$$

and our problem reduces to an eigenvalue problem for the positive semidefinite matrix  $L$  (notice that  $Ly = 0$  whenever all components of  $y$  are equal). The requested projection to  $n$  points in  $\mathbb{R}^d$  for all voxels  $i$  is then given by viewing the  $d$  normalized eigenvectors with the smallest non-zero eigenvalues as  $n$  points in  $\mathbb{R}^d$ .

In our experiments, the standard  $k$ -means technique is applied to the first three eigenvectors  $y$  (i.e.  $d = 3$ ) for clustering. All the synthetic data consist of  $n = 256$  voxels.

The individual steps of the entire clustering procedure are listed in algorithm 4. The results on the following synthetic image for various projections and metrics are illustrated in Figure 3.

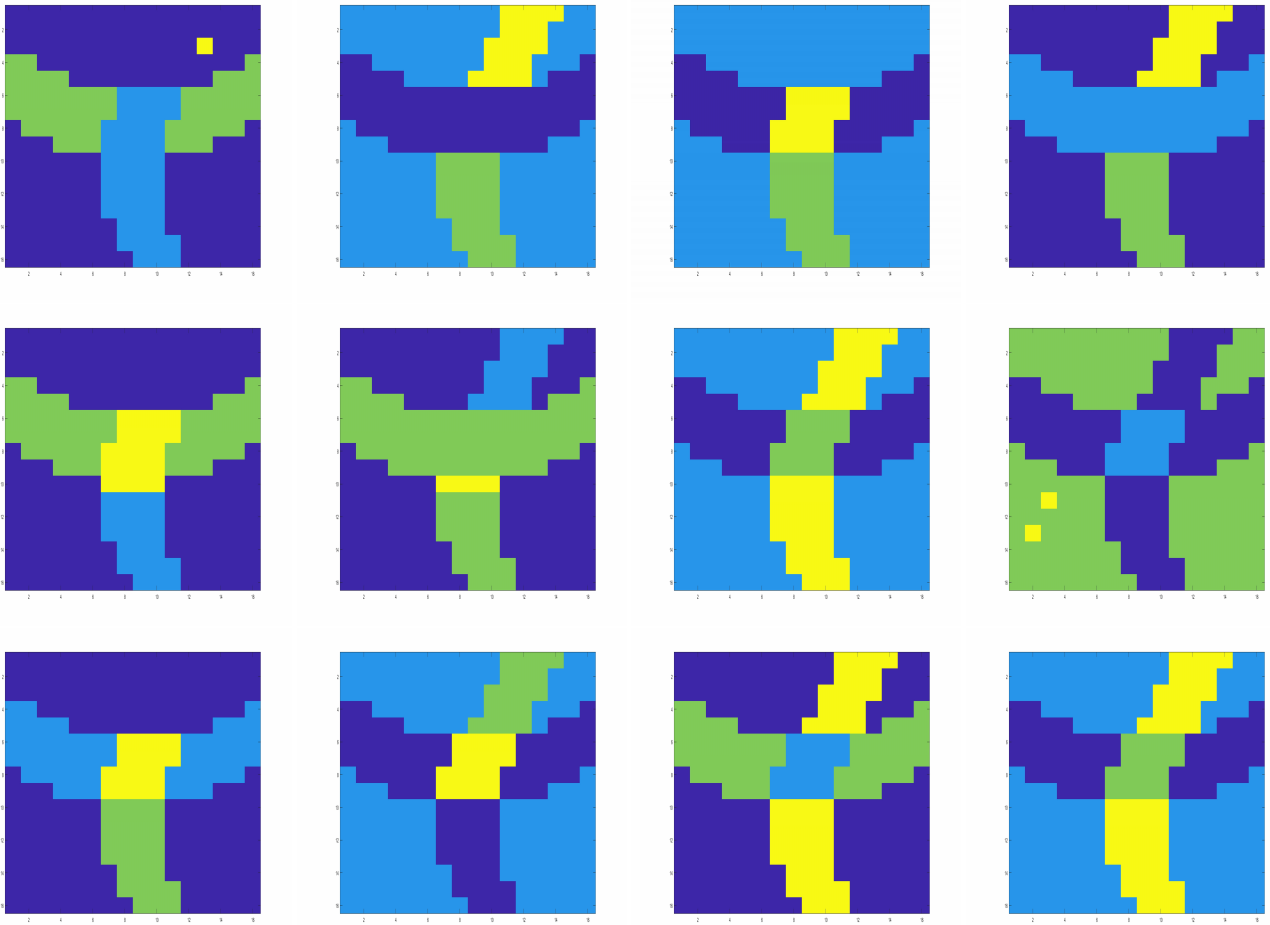
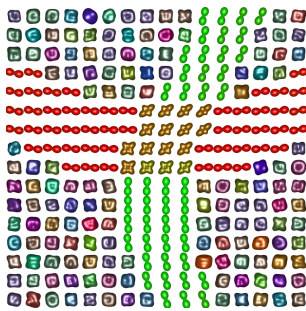


Fig. 3: Results with diverse metrics and projections. The rows show the LogE, SQ, and slerpSQ metrics, from top to bottom, while the L projection appears in the first two columns, first without and then with the noise, and finally, the last two columns show the same for the D projection. The colors are chosen randomly.



The image was created with additional random background noise (introducing randomness in partial fractions of the voxels, still nearly anisotropic), cf. [39]. The corresponding image without noise shows the same voxels in the fibers and uniform anisotropic background.

#### Algorithm 4. Laplacian Eigenmap Clustering

*Input:* Field of  $n$  fourth order tensors lying in the manifold embedded in high dimension.

*Output:* Segmentation of voxels into regions with background, structural fibers and their intersections.

1. Project the 4th order tensors onto 2nd order ones by one of the methods described above.
2. Compute the affinity matrix  $W$  with weights given by (10), using the similarity measure as approximation for the geodesic distance.
3. Compute the graph Laplacian (11) of the affinity matrix.
4. Perform the eigen decomposition with respect to  $L$  and take the first three normalized eigenvectors, representing the voxels as the set  $S$  of  $n$  points in  $\mathbb{R}^3$ .
5. Perform  $k$ -means clustering on the projection  $S \subset \mathbb{R}^3$ .

Our experiments revealed much higher robustness when the similarity measure involves the slightly blown up Euclidean distance between the neighboring voxels, both with respect to the curvature of the fibers and the noise in the data.

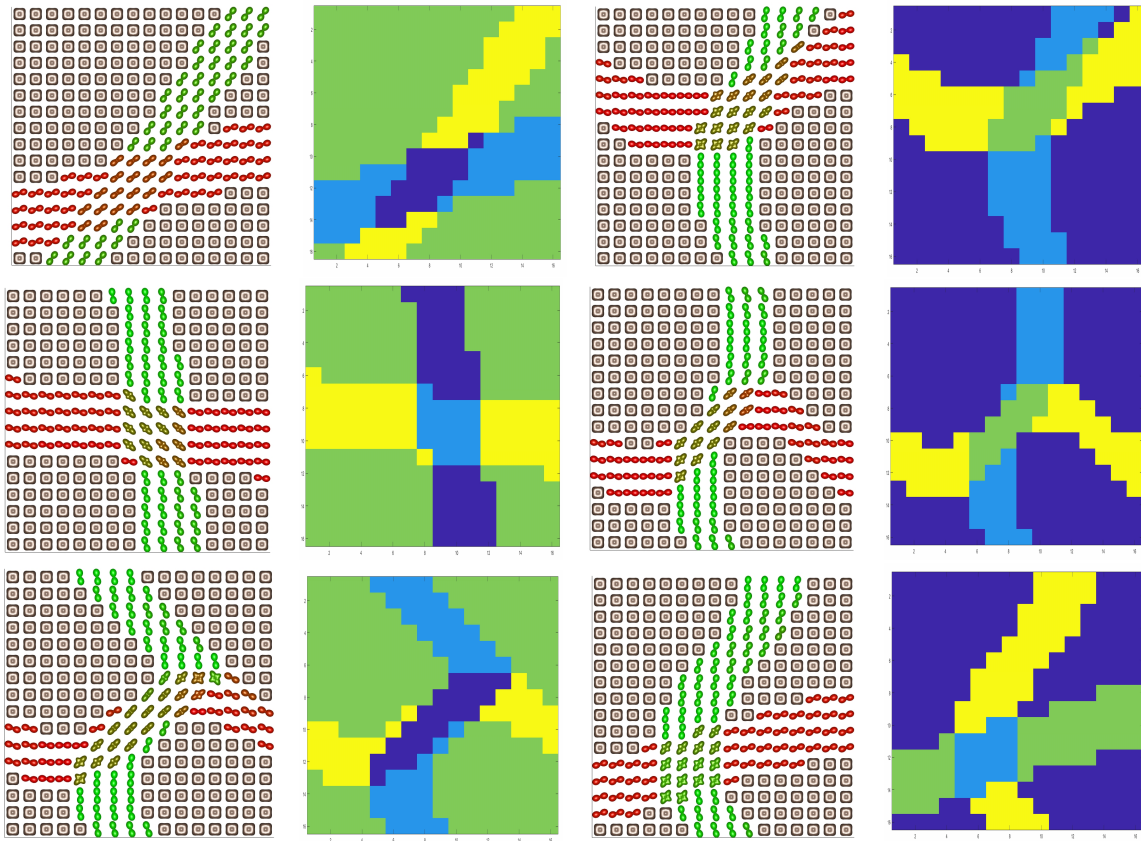


Fig. 4: The pictures show various original synthetic images (without any noise) followed by the segmentation into four regions using the slerpSQ metric, D projection, and the uniform approach via Algorithm 4.

On Figure 4, six configurations of synthetic images, with two fibers each, are segmented successfully using slerpSQ and D projection.

The Figure 5 illustrates the effectivity of the segmentation on a (noisy) real image, with two or four regions. Because of different shape and resolution of the data, the parameter  $w_e$  in (10) was tuned up appropriately.

We have also tested the robustness of the clustering with respect to the noise added to the background data under different projections and metrics. We created a bank of 15 different configurations with 20 randomly changed backgrounds each. The table on the left provides the overview of the accuracy of average segmentations achieved. For two crossing fibers there are 4 parts of them to be recognized. If at least three of these parts are decided correctly in the segmented regions, we assign the accuracy value 1. It turned out that the Eigentensor projection does not obey the positive definiteness once the background noise is added. Thus the experiment completely failed for this projection. The table on the right compares the SQ and slerpSQ metric under the D projection with the more strict accuracy evaluation when the accuracy value is 1 only in the case of all four regions segmented properly.

	L	D	E
SQ	0.66	0.97	fails
SlerpSQ	0.69	0.98	fails
LogE	0.763	0.67	fails

	D
SQ	84.33
SlerpSQ	86.33

## 5.2 Deformable Models

We have also tested the effectiveness of the similarity measures based on slerpSQ and SQ distances in other situations. In particular we employ the Algorithms 1 and 2 for curve segmentation. Partial results were reported in [46].

In deformable models/snakes, [47] introduced an energy function to evolve the curve, which was fast but has difficulty in handling topological changes. Evolution of curves is guided by curvature motion and edge function. In [48, 49, 50] edges act as evolving and stopping terms for the curve as the value of the edge function is zero near the boundaries of the object.

The disadvantage of these edge based methods is their inability to deal with noise, because the Gaussian is also smoothing the boundaries in the process of smoothing the noise. Other shortcoming is that it requires the initial curve to be placed near to the boundary of the object of interest.

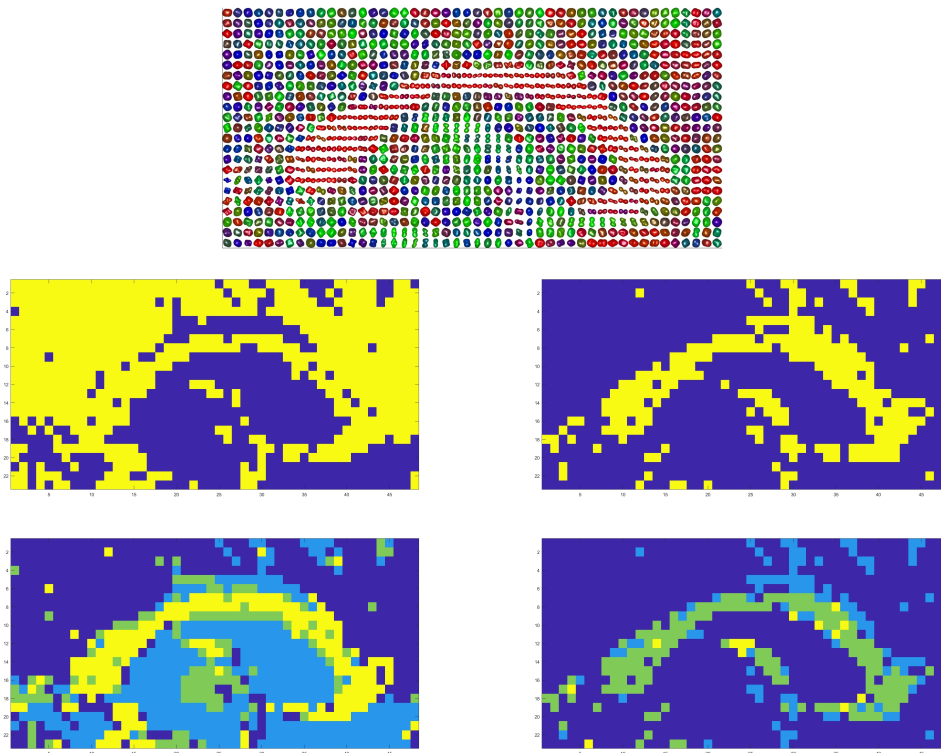


Fig. 5: Results on noisy real image of Corpus Callosum segmented into two and four regions under SQ metric (left) and slerpSQ (right). The real image is obtained with single shell,  $b=1500s/mm^2$ , 64 gradient directions voxel of size  $2mm \times 2mm \times 2mm$ , with total size  $114 \times 114 \times 70$ . Our algorithms run on cut out section of Corpus Callosum with size  $44 \times 48 \times 23$ . Slice with  $x = 30$  is shown here.

In [51], Osher and Sethian used level-sets to deal with the topological changes during curve evolution, i.e., the evolving curve is embedded in a hypersurface in a higher dimensional space.

The Chan-Vese model, [52], is based on the Mumford-Shah model, [53], and it evolves the curve without requiring edges as stopping conditions. Their formulation uses the energy based on first moments of energy distribution in the interior and exterior regions of the curve, which is represented as a level of a surface. If  $\phi$  is the defining equation of the surface having the curve as its zero level, then the curve evolution is governed by the gradient of  $\phi$ ,

$$\frac{\partial \phi}{\partial t} = |\nabla \phi| F \quad (12)$$

where  $F$  is the speed of the curve evolution. Various choices of the function  $F$  exist in the literature.

We propose to exploit the spectral quaternion based similarity measures in the approach. In our experiments, we use the Mumford-Shah energy functional based model, where  $F$  is the curvature of the level curve passing through the point in question. The minimization of the Mumford-Shah energy pushes the evolving curve to boundary of the object. It en-

ables to segment the objects with or without boundaries, and with even discontinuous boundaries, and it is robust to noise.

Region based techniques work well for the objects with uniform features but fail if subregions of the object have non-uniformity. Aside of the global techniques, we use the local energy functional for fiber bundle segmentation for 3D DTI, [54,55]. In the original work, the authors used Log-Euclidean metric and they advocated the improvement under a better similarity measures/metric. In [56], the authors used variational technique on diverse manifold valued images.

We use the SQ and slerpSQ similarity measures for evolution of global curve to test segmentation of curved fiber structures. The results indicate much better performance of the algorithm compared to the LogE metric, cf. Fig. 6.

## 6 Results and discussions

We have tested two segmentation methods, the Riemannian spectral clustering and the deformable models, on 2nd order projections of 4th order tensors, mainly on synthetic images. The framework [39] is used to obtain multiple fiber configurations. Various shapes of fibers and their intersections were

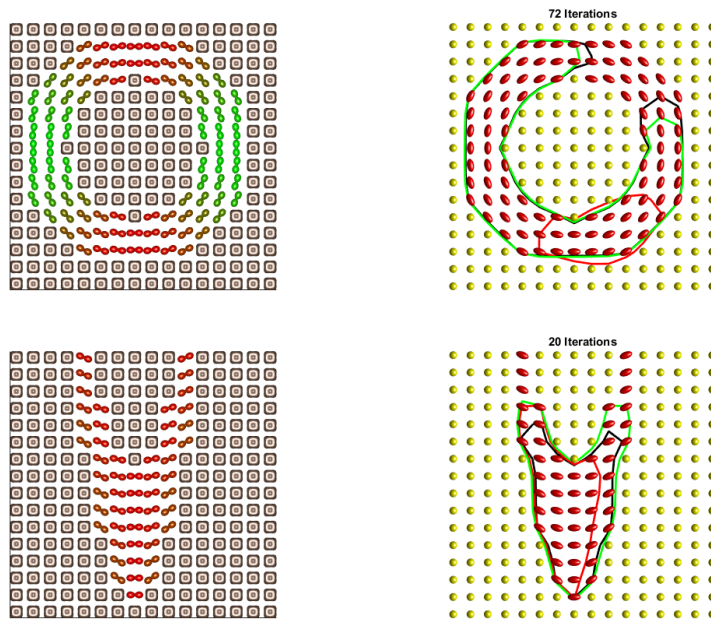


Fig. 6: We illustrate the behavior of the deformable model algorithm on two synthetic images (one with constant curvature of the edges, the other with high curvature parts). The global version of the contour evolution is applied to the second order tensor fields obtained by the D projections from the fourth order ones. Green curves shows the results under the slerpSQ metric, black curves stay for SQ, while the results for LogE are red. In both cases performance under slerpSQ and SQ is comparable, whereas LogE is unable to evolve in high curvature regions, but slerpSQ runs faster in such cases.

tested. We checked the applications of three projections and three diverse metrics on many simulated images.

While the linear projection L and the eigentensor projection E are well known, we add the simple D projection, based on the observation that the diagonal blocks in the flattened 4th order tensors are always positive definite. We also suggest to use the slerpSQ modification of the SQ metric (while the SQ metric was proposed in [42], the former one was used e.g. in gaming).

Figure 3 illustrates the results using two projections D and L and the three metrics LogE, SQ, and slerpSQ, with and without background noise. Notice, the E projection was not involved since it failed with the noisy images. We also created a bank of 15 images, with random noise added 20 times each, and compared the quality of the segmentations, see the two tables above.

Moreover, we tested the deformable models with the same projections and metrics.

As expected, both the spectral quaternion based metrics performed much better in both models, with slightly better results for slerpSQ.

We also implemented a modification of the affinity matrix in the LE map definition. The improvement consists in increasing the considered distance of very near voxels slightly. At the same time, we introduced uniform normalization of constants in the definition of the affinity matrix.

As a consequence, the method got much more robust and allows to compare the results uniformly.

For some cases, in spite of spatial regularization, inaccurate extractions are to be expected. Involvement of an expert (user interaction) is capable to resolve the problem by propagating affinities across the regions as in [23]. We shall come back to this approach in near future.

Another perspective enhancement of our study is to lift the 3D images to the extended 5D space of positions and orientations (the quotient of the group of Euclidean motions), [57]. In this larger space, we may define a metric suitable for connectivity measurement in DW-MRI images in a form of sub-Riemannian metric, [58], or a sub-Finslerian quasi metric, [59].

Diffusion Kurtosis Imaging (DKI) is a promising modality in classification of damage of tissues due to disease and injury. DKI data is useful in segregating regions of white matter, gray matter, and Cortico Spinal Fluid (CSF), [60]. Our work can be of importance in segmentation of DKI data as DKI involves both 2nd order diffusion tensors and 4th order kurtosis tensors. We shall come back to this in future work.

**Acknowledgements** The authors are grateful to Lubomír Vojtíšek and CEITEC labs of the Masaryk University for providing real dwMRI data. The authors also very much appreciate many useful comments

and suggestions by the anonymous referees which led to tremendous improvement of the paper as well as motivation for further work.

## References

1. Basser P., Mattiello J., LeBihan D., Estimation of the effective self-diffusion tensor from the NMR spin echo. *Journal of Magnetic Resonance B*. 103(3): 247–254 (1994)
2. Barmpoutis A., Hwang M.S., Howland D., Forder J.R., Vemuri B.C., Regularized positive-definite fourth order tensor field estimation from DW-MRI. *NeuroImage*. 45(1 Suppl.): S153–S162 (2009)
3. Fletcher P.T., Geodesic regression and the theory of least squares on Riemannian manifolds. *Int. J. Comput. Vis.*, 105 pp. 171–185 (2013)
4. Fletcher P.T., Joshi S., Principal geodesic analysis on symmetric spaces: Statistics of diffusion tensors. in: Milan Sonka, Ioannis A. Kakadiaris, Jan Kybic (Eds.), *Computer Vision and Mathematical Methods in Medical and Biomedical Image Analysis*, Lecture Notes in Computer Science, vol. 3117, Springer, Berlin, Heidelberg pp. 87–98 (2004)
5. Fletcher P.T., Conglin Lu, Sarang Joshi, Statistics of shape via principal geodesic analysis on lie groups. *Proceedings of the 2003 IEEE Computer Society Conference on Computer Vision and Pattern Recognition (Washington, DC, USA), CVPR'03*, IEEE Computer Society, pp. 95–101 (2003)
6. Krajsek K., Menzel M.I., Scharf H., A Riemannian Bayesian Framework for Estimating Diffusion Tensor Images. *Int. J. Comput. Vis.* 120: p. 272 (2016)
7. Pennec X., Fillard P., Ayache N., A Riemannian Framework for Tensor Computing. *International Journal of Computer Vision*, (Springer) 66(1):41–66 (2006)
8. Lenglet C. et. al., A Riemannian Approach to Diffusion Tensor Images Segmentation. *Information Processing in Medical Imaging*, pp. 591–602 (2005)
9. Wedeen V.J., Hagmann P., Tseng W.Y., Reese T.G., Weisskoff R.M., Mapping complex tissue architecture with diffusion spectrum magnetic resonance imaging. *Magn. Reson. Med.* 54(6): 1377–86 (2005)
10. Tuch D.S., Q-ball imaging. *Magn. Reson. Med.* 52(6): 1358–72 (2004)
11. Rousson M., Lenglet C., Deriche R., Level set and region based surface propagation for diffusion tensor MRI segmentation. *Computer vision and mathematical methods in medical and biomedical image analysis*. Springer, Berlin, Heidelberg, 2004. 123–134.
12. Guo, W., Yunmei C., Qingguo Z., A geometric flow-based approach for diffusion tensor image segmentation. *Philosophical Transactions of the Royal Society of London A: Mathematical, Physical and Engineering Sciences* 366.1874: 2279–2292 (2008)
13. Tuch D.S., Weisskoff R.M., Belliveau J.W., Wedeen V.J., High angular resolution diffusion imaging of the human brain. In: *Proc. of the 7th Annual Meeting of ISMRM, Philadelphia, PA*, p. 321 (1999)
14. Tuch D.S., Reese T.G., Wiegell M.R., Wedeen V.J., Diffusion MRI of complex neural architecture. *Neuron* 40, 885–895 (2003)
15. McGraw T., Vemuri B., Yeziarski R., Mareci T., Segmentation of high angular resolution diffusion MRI modeled as a field of von Mises–Fisher mixtures. *European Conference on Computer Vision* pp. 463–475 (2006)
16. Jonasson L., Bresson X., Thiran J.P., Wedeen V.J., Hagmann P., Representing diffusion MRI in 5-D simplifies regularization and segmentation of white matter tracts. *IEEE Trans. Med. Imaging*. 26(11): 1547–54 (2007)
17. Wassermann D., Descoteaux M., Derich R., Diffusion maps segmentation of magnetic resonance q-ball imaging. *Computer Vision, 2007. ICCV 2007. IEEE 11th International Conference on*. IEEE, (2007)
18. Descoteaux M., Deriche R., High angular resolution diffusion MRI segmentation using region-based statistical surface evolution. *Journal of Mathematical Imaging and Vision* 33.2: 239–252 (2009)
19. Goh A., Lenglet C., Thompson P., Vidal R., A nonparametric Riemannian framework for processing High Angular Resolution Diffusion Images (HARDI) *Conference on Computer Vision and Pattern Recognition* (2009)
20. Goh A., Lenglet C., Thompson P.M., Vidal R., A nonparametric Riemannian framework for processing high angular resolution diffusion images and its applications to ODF-based morphometry. *NeuroImage Volume 56, Issue 3*, pp. 1181–1201 (2011)
21. Awate S.P., Zhang H., Gee G.J., A fuzzy, nonparametric segmentation framework for DTI and MRI analysis: With applications to dti-tract extraction. *IEEE Transactions on Medical Imaging*, 26(11): 1525–1536 (2007)
22. Cetingul H.E., Vidal R., Sparse Riemannian manifold clustering for HARDI segmentation. *IEEE International Symposium on Biomedical Imaging*; pp. 1750–1753 (2011)
23. Cetingul H.E., Wright M.J., Thompson P.M., Vidal R., Segmentation of high angular resolution diffusion MRI using sparse riemannian manifold clustering. *IEEE Trans Med Imaging* (2014)
24. Barmpoutis A., Vemuri B.C., A Unified Framework for Estimating Diffusion Tensors of any order with Symmetric Positive-Definite Constraints. In the *Proceedings of ISBI*. (2010)
25. Frank, L.R., Characterization of anisotropy in high angular resolution diffusion weighted MRI. *Magn. Reson. Med.* 47 1083–1099 (2002)
26. Özarslan E., Mareci T.H., Generalized DTI and analytical relationships between DTI and HARDI. *MRM*. Nov; 50(5), 955–965 (2003)
27. Descoteaux M., Angelino E., Fitzgibbons S., Deriche R., Apparent diffusion coefficients from high angular resolution diffusion imaging: Estimation and applications. *Magnetic Resonance in Medicine: An Official Journal of the International Society for Magnetic Resonance in Medicine* 56, no. 2: 395–410 (2006)
28. Liu C., Bammer R., Moseley M.E., Limitations of apparent diffusion coefficient-based models in characterizing non-gaussian diffusion. *Magn. Reson. Med.* 2005 Aug;54(2):419–428 (2005)
29. Wedeslasiess Y.T., Barmpoutis A., Atkins M.S., Symmetric positive-definite Cartesian tensor orientation distribution functions (CT-ODF). *Med. Image Comput. Assist. Interv.* 13 (Pt 1):582–589 (2010)
30. Le Bihan D., Apparent diffusion coefficient and beyond: what diffusion MR imaging can tell us about tissue structure. *Radiology* Aug; 268(2):318–22 (2013)
31. Ghosh A., Papadopoulo T., Deriche R., Biomarkers for HARDI: 2nd & 4th order tensor invariants. In: *ISBI*, pp. 2629 (2012).
32. Ghosh A., Papadopoulo T., Deriche R., Generalized invariants of a 4th order tensor: building blocks for new biomarkers in dMRI. *Proceedings of the Computation Diffusion MRI Workshop at the MICCAI Conference* (2012)
33. Nice F., Gur Y., Johnson C.R., Generalized HARDI invariants by method of tensor contraction. In: *IEEE Symposium on Biomedical Imaging*. Beijing, China (2014)
34. Barmpoutis A. et al. Regularized Positive-Definite Fourth-Order Tensor Field Estimation from DW-MRI. *NeuroImage*, Vol. 45(1 sup.1), Page(s): 153–162 (2009)
35. Ghosh A., Deriche R., Moakher M., Ternary quartic approach for positive 4th order diffusion tensors revisited. *ISBI*, 618–621 (2009)
36. Basser P.J., Pajevic S., Spectral decomposition of a 4th-order covariance tensor: Applications to diffusion tensor MRI, *Signal Processing*, Volume 87, Issue 2, (2007)

37. Moakher M., Fourth-order cartesian tensors: Old and new facts, notions and applications. *The Quarterly Journal of Mechanics and Applied Mathematics*. (2008)
38. Jayachandra M.R., Rehbein N., Herweh C., Heiland S., Fiber Tracking of Human Brain Using Fourth-Order Tensor and High Angular Resolution Diffusion Imaging. *Magnetic Resonance in Medicine* 60:1207–1217 (2008)
39. Barmpoutis A. et al., Adaptive kernels for multi-fiber reconstruction. In the Proceedings of IPMI, pp. 338-349 (2009)
40. Arsigny V. et. al., A Log–Euclidean framework for statistics on diffeomorphisms, Proc. of the 9th International Conference on Medical Image Computing and Computer Assisted Intervention (MICCAI'06) (2006)
41. Tschumperle, D., Deriche, R., Diffusion tensor regularization with constraints preservation. *Computer Vision and Pattern Recognition. IEEE Computer Society Conference on*, 1, p. 948 (2001)
42. Collard A., Bonnabel S., Phillips C., Sepulchre R., An anisotropy preserving metric for DTI processing. *International Journal of Computer Vision*, Volume 107 Issue 1, 58-74 (2014)
43. Huynh D.Q., Metrics for 3D rotations: comparison and analysis. *J. Math. Imaging Vis.*, 35 (2) pp. 155-164 (2009)
44. Schwartzman A., Lognormal Distributions and Geometric Averages of Symmetric Positive Definite Matrices. *International Statistical Review*, 84, 3, 456486 (2016)
45. Belkin M., Niyogi P., Laplacian eigenmaps for dimensionality reduction and data representation. *Neural Comput.* 15(6), 1373–1396 (2003)
46. Kaushik, S., Slovák, J., DTI Segmentation Using Anisotropy Preserving Quaternion Based Distance Measure, in Campilho et al. (Eds.): ICIAR 2018, LNCS 10882, pp. 81–89 (2018)
47. Kass M., Witkin A., Terzopoulos D., Snakes: active contour models. *Int. J. Comput. Vis.*, vol. 1, pp. 321–331 (1987)
48. Malladi R., Sethian J.A., Vemuri B.C., Shape modeling with front propagation: a level set approach. *IEEE Trans. Pattern Anal. Mach. Intell.*, 17 (2) pp. 158–175 (1995)
49. Caselles V., Kimmel R., Sapiro G., Geodesic active contours. *Int. J. Comput. Vision*, 22 (1) pp. 61–79 (1997)
50. Malladi R., Sethian J.A., Vemuri B.C., Shape modeling with front propagation: a level set approach. *IEEE Trans. Pattern Anal. Mach. Intell.*, 17 (2) pp. 158–175 (1995)
51. Osher S., Sethian J., Fronts propagating with curvature-dependent speed: algorithms based on Hamilton-Jacobi formulations. *J. Comput. Phys*, vol. 79, pp. 12–49 (1988)
52. Chan T., Vese L., Active contours without edges. *IEEE Trans. Image Process.*, vol. 10, no. 2, pp. 266–277 (2001)
53. Mumford, D., Shah, J., Optimal approximation by piecewise smooth functions and associated variational problems. *Comm. Pure Appl. Math.* 42 577–685 (1989)
54. Lankton S., Tannenbaum A., Localizing region-based active contours. *IEEE Trans. Image Process.*, 17 (11) pp. 2029–2039 (2008)
55. Lankton S., Melonakos J., Malcolm J., Dambreville S., Tannenbaum A., Localized statistics for DW-MRI fiber bundle segmentation. 805, 2016. In Proc. 21st CVPR Workshops, pages 1–8 (2008)
56. Bansal S., Tatu A., Active Contour Models for Manifold Valued Image Segmentation. *J. Math. Imaging Vis.* 52, 2, 303–314 (2015)
57. Duits R., Dela Haije T., Creusen E., Ghosh A., Morphological and Linear Scale Spaces for Fiber Enhancement in DW-MRI. *JMIV*, 46(3), pp. 326–368 (2013)
58. Duits R., Ghosh A., Dela Haije T., Mashtakov A., On sub-Riemannian geodesics in  $SE(3)$  whose spatial projections do not have cusps. *JDCS*, 22(4), pp. 771–805 (2016)
59. Portegies J., Meesters S., Ossenblok P., Fuster A., Florack L., Duits R., Brain Connectivity Measures via Direct Sub-Finslerian Front Propagation on the 5 D Sphere Bundle of Positions and Directions, preprint (2018)
60. Bista S., Zhuo J., Gullapalli R.P., Varshney A., Visual knowledge discovery for diffusion kurtosis datasets of the human brain. in *Visualization and Processing of Higher Order Descriptors for MultiValued Data*. Cham, Switzerland: Springer, 2015, pp. 213–234 (2015)